# II

# SURFRESIDE$^2$: An Ultrahigh Vacuum System for the Investigation of Surface Reaction Routes of Interstellar Interest

A new ultrahigh vacuum experiment is described to study atom and radical addition reactions in interstellar ice analogues for astronomically relevant temperatures. The new setup - SURFRESIDE$^2$ - allows a systematic investigation of solid state pathways resulting in the formation of molecules of astrophysical interest. The implementation of a double beam line makes it possible to expose deposited ice molecules to different atoms and/or radicals sequentially or at the same time. Special efforts are made to perform experiments under fully controlled laboratory conditions, including precise atom flux determinations, in order to characterize reaction channels quantitatively. In this way we can compare and combine different surface reaction channels with the aim to unravel the solid state processes at play in space. Results are constrained in situ by means of a Fourier transform infrared spectrometer and a quadrupole mass spectrometer using RAIRS and TPD, respectively. The performance of the new setup is demonstrated on the example of carbon dioxide formation by comparing the efficiency through two different solid state channels ($CO + OH \rightarrow CO_2 + H$ and $CO + O \rightarrow CO_2$) for which different addition products are needed. The potential of SURFRESIDE$^2$ to study complex molecule formation, including nitrogen containing (prebiotic) compounds, is discussed.

S. Ioppolo, G. Fedoseev, T. Lamberts, C. Romanzin and H. Linnartz, 2013, Rev. Sci. Instrum., 84, 073112

## 2.1 Introduction

More than 180 different molecules, not including isotopes, have been identified in the space around and in between stars, *i.e.*, the circum- and interstellar medium. It is commonly accepted that this chemical diversity is the outcome of a complex interplay between reactions in the gas phase and on icy dust grains. The latter have been identified in space and are currently topic of dedicated laboratory simulations. During the last decade, the introduction of ultrahigh vacuum systems has improved our understanding of molecule formation in the solid state for astronomically relevant temperatures, introducing a new research field: solid state astrochemistry. Fully controlled laboratory experiments have shown that new molecules form in and on the ices upon thermal processing; energetic processing induced by vacuum UV light, X-rays, cosmic rays, and electrons; and non-energetic processing like atom bombardment. Meanwhile it has been confirmed that, except for CO that is efficiently formed in the gas phase, the bulk of interstellar ices (*i.e.*, water, carbon dioxide, methanol, formaldehyde, formic acid, ammonia) is formed in the solid phase through surface reactions (Hiraoka *et al*. 1994, Watanabe & Kouchi 2002a, Fuchs *et al.* 2009, Miyauchi *et al*. 2008, Ioppolo *et al.* 2008, Matar *et al.* 2008, Dulieu *et al*. 2010, Oba *et al*. 2010a, Ioppolo *et al*. 2011a, Noble *et al*. 2011, Ioppolo *et al*. 2011b, Loeffler *et al*. 2005, Ioppolo *et al*. 2009, Raut & Baragiola 2011, Fulvio *et al.* 2012, Linnartz *et al*. 2011). The focus in this paper is on a new UHV setup able to study atom and radical addition reactions in interstellar ices. In recent years, the formation of a number of molecules was proven upon CO, $O_2$, and $O_3$ hydrogenation, yielding $H_2CO$, $CH_3OH$, $H_2O_2$, and most importantly $H_2O$ (Watanabe & Kouchi 2002a, Fuchs *et al*. 2009, Miyauchi *et al*. 2008, Ioppolo *et al*. 2008, Matar *et al*. 2008, Ioppolo *et al*. 2010, Cuppen *et al*. 2010, Mokrane *et al*. 2009, Romanzin *et al*. 2011). Also more complex species such as ethanol ($CH_3CH_2OH$) upon ethanal hydrogenation (Bisschop *et al*. 2007a) and hydroxylamine ($NH_2OH$) following NO hydrogenation (Congiu *et al*. 2012a, Congiu *et al*. 2012b, Fedoseev *et al*. 2012) have been shown to form in the solid state. The latter is a potentially important prebiotic precursor of glycine and β-alanine (Blagojevic *et al*. 2003). Not only reaction products have been determined in this way, but also the underlying reaction schemes have been characterized as well as their dependence on a number of variable parameters, such as temperature, H-atom flux, ice morphology (mixing ratio, thickness, and structure). It is found that the chemical processes involved are far from trivial and this only gets more complicated when ice mixtures are studied (Ioppolo *et al*. 2009a, Ioppolo *et al*. 2009b, Fedoseev *et al*. 2012).

The majority of these experiments have been realized using setups in which a single atom/radical source is available for ice processing. This comes with restrictions, as reactions are limited to one specific impacting species. A second beam line offers much

additional potential, *i.e.*, the simultaneous or sequential bombardment of an ice with different constituents, for example H- and D-atoms to study isotopic effects, or H- and O-atoms or H- and N-atoms to combine hydrogenation with oxygenation or nitrogenation reactions, in order to grow more and more complex molecules. The new SURFace REaction SImulation DEvice allows ice deposition using two deposition lines and comprises two separate atom beam lines for ice processing. In the following, the setup is denoted as SURFRESIDE$^2$. This next generation UHV setup has been constructed with the specific aim to “unlock the chemistry of the heavens", by studying molecular complexity in interstellar ice analogues upon atom/radical addition reactions.

The focus here is on a quantitative characterization of the experimental properties of SURFRESIDE$^2$, using a new approach to fully characterize atom fluxes. Its performance is demonstrated through different reactions in the ice resulting in $CO_2$ formation. Solid carbon dioxide is found in relatively large abundances w.r.t. water ice, typically at the level of 13−29% towards high- and low-mass stars, see Oberg *et al*. (2011). Consequently, it offers an excellent tracer to characterize the chemical history of the interstellar medium, provided that its formation scheme is well understood.

### 2.2 System description

SURFRESIDE$^2$ consists of three distinct UHV chambers (Fig. 2.1). In the main chamber, ices are deposited with monolayer precision and processed at astronomically relevant temperatures. Reflection-Absorption Infrared Spectroscopy (RAIRS) and Temperature Programmed Desorption (TPD) are used as analytical tools to characterize the ice composition. In the other chambers different atom sources are mounted for the controlled production of well-characterized atom (molecular) beams. Shutters separate the beam line chambers from the main chamber and allow an independent operation of the individual beam lines.

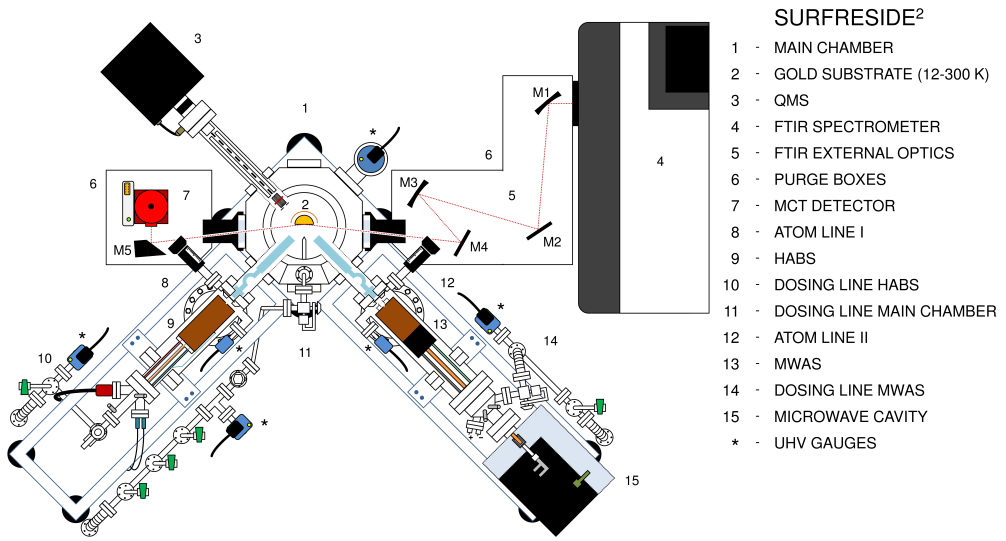


**Figure 2.1.** A schematic top-view of the experimental apparatus.

### 2.2.1 Main chamber

The custom-made ultrahigh vacuum 304 stainless steel main chamber has a diameter of 30 cm and is provided with eight lateral CF 35, two lateral CF 16, one top CF 63 and one bottom CF 200 flange connections (#1 in Fig. 2.1). A gate valve connects the bottom-flange with a 260 l/s (for $N_2$) turbomolecular pump (Pfeiffer Vacuum, TMU 261P). The CF 35 lateral flanges are used to connect the main chamber to the two atom lines (#8 and #12 in Fig. 2.1), an active cold cathode transmitter (Pfeiffer Vacuum, IKR270) for pressure readings in the $5 \cdot 10^{-11}$ - 0.01 mbar range, and a quadrupole mass spectrometer (QMS; Spectra - Microvision Plus; #3 in Fig. 2.1). Two CF 35 windows are used for in- and out-going light from a Fourier transform infrared spectrometer (FTIR; Agilent Technologies Cary 600 Series; #4 in Fig. 2.1). The two CF 16 flanges are used as inlet for a double ice deposition dosing line (#11 in Fig. 2.1), while a differentially-pumped (Leybold Vacuum, TW 300) $\vartheta$ rotatable stage (0°-360°) connects the top-flange to a helium closed-cycle refrigerator (ASR Inc.; #2 in Fig. 2.1).

The room temperature base pressure of the main chamber is in the low $10^{-10}$ mbar regime. An optically-flat gold-coated copper substrate (2.5 x 2.5 $cm^2$) is placed in the center of the main chamber and is in thermal contact with the cold finger of the helium closed-cycle cryostat. The gold surface is not representative for interstellar grain surfaces, but it is an effective heat conductor, highly reflective in the mid-infrared, and chemically

inert, *i.e.*, the substrate plays no role in catalyzing chemical reactions or processes at the substrate surface. Moreover, ice thicknesses are typically more than ten monolayers, reducing the role of the substrate. Therefore, it is well suited to study interstellar relevant reaction routes that occur on and in ice samples. The substrate temperature is varied between 12 and 300 K with a relative precision of 0.5 K through a cryogenic temperature controller (LakeShore model 340). To achieve temperatures as low as 12 K an aluminum thermal shield kept at ~77 K surrounds the cold finger and the back-side of the sample. The temperature of the sample is changed and monitored by means of heating wires and thermocouples, respectively. The heating wires are mounted around the cold finger close to the substrate, while the two KP-type thermocouples are connected above and below the gold substrate. The absolute temperature accuracy is better than 2 K. This is checked by monitoring the well known desorption temperature of volatile species like for instance CO, $N_2$, and $O_2$ (Acharyya *et al*. 2007).

An all metal high-vacuum stainless steel ice deposition dosing line is used to prepare, store and introduce gas mixtures into the main chamber. The pressure in the deposition dosing line is monitored mass independently by means of an active capacitance transmitter (Pfeiffer Vacuum, CMR361) in the range between 0.1 and 1100 mbar. Lower pressures are monitored with an active Pirani transmitter (Pfeiffer Vacuum, TPR280) ($5\cdot10^{-4}$ to 1000 mbar). The deposition dosing line is first pre-pumped with a diaphragm pump (ABM, VDE 0530) and then with a 180 l/s (for $N_2$) turbomolecular pump (Pfeiffer Vacuum, TPH 180H) to reach low pressures ($<5\cdot10^{-4}$ mbar). Gaseous species are admitted into the main chamber through a dosing line comprising of two separate all-metal leak valves connected to gas reservoirs. Therefore, different gases can be prepared and stored in two different sections of the dosing line and then deposited separately or simultaneously onto the gold substrate. Deposition proceeds under an angle of 90° and 68°, respectively, and with a controllable flow between $10^{-8}$ and $10^{-7}$ mbar $s^{-1}$, where $1.3\cdot10^{-6}$ mbar $s^{-1}$ corresponds to 1 Langmuir (L). Gas-phase species are monitored during deposition mass spectrometrically by means of the QMS, which is placed behind the substrate and mounted opposite to one of the two atom lines.

### 2.2.2 Analytical tools

Ices are monitored *in situ* by means of RAIRS using the FTIR, which covers the range between 4000 and 700 cm−1 (2.5−14 $\mu$m). A spectral resolution between 1 and 4 $cm^{-1}$ is generally used and between 128 and 512 scans are co-added. The infrared beam coming from the FTIR is slowly diverging. Therefore, a series of $\lambda/4$ precision gold-coated mirrors (Edmund Optics and Thorlabs) is used to focus the beam onto the gold substrate (#5 in Fig. 2.1). The first one (M1) is a spherical mirror with a diameter of 76.2 mm and an effective

focal length (EFL) of 762 mm. This mirror is used to gently converge the beam. The second (M2) and the fourth mirror (M4) are flat mirrors, while the third one (M3) is a spherical mirror with a diameter of 75.0 mm and an EFL of 500 mm. The latter focusses the beam onto the substrate with a glancing angle of ~8°. The main chamber mounts two Zinc Selenide (ZnSe) CF 35 view ports that act as a vacuum seal and allow the IR beam to enter and leave the chamber with a transmission >95% in the range between 4−20 $\mu$m. The out-going beam is then focussed into a narrow band and LN2 cooled Mercury Cadmium Telluride (MCT; #7 in Fig. 2.1) detector by means of a 90° off-axis parabolic gold-coated mirror (M5) with a diameter of 50.8 mm and a reflected EFL of 50.8 mm. The external optics and the detector are mounted in metal boxes (#6 in Fig. 2.1). These boxes as well as the FTIR are purged with dry-air to minimize atmospheric absorptions.

Two different experimental procedures are applied when using the FTIR. During pre-deposition experiments, ices are first deposited onto the gold substrate and subsequently exposed to atoms. To detect newly formed stable solid species, RAIR difference spectra are acquired during atom exposure with respect to a background spectrum of the initial deposited ice. In co-deposition experiments, molecules and atoms are simultaneously deposited onto the substrate. The formation of intermediate species and final products is controlled by changing the deposited molecule/atom ratio. In this case, RAIR difference spectra are acquired during co-deposition with respect to a background spectrum of the bare gold substrate.

At the end of the atom exposure a TPD experiment can be performed: the sample is heated linearly (*i.e.*, with a constant rate between 0.1 and 10 K/min) till the ice is fully desorbed. The thermal desorption can be followed spectroscopically by using the FTIR. Alternatively, the sample can be turned 135° to face the QMS. In this way, gas-phase species thermally desorbed from the ice are monitored mass spectrometrically. The desorbed species are recorded as a function of temperature by the QMS, which produces a signal proportional to the number of incoming molecules as a function of their mass to charge ratio (m/z). The incoming molecules first enter the ion source of the QMS, where they are ionized through electron bombardment by electrons released from a hot filament. The resulting ions are then focussed, selected and directed onto a Faraday detector, which collects the ions directly, allowing the ion current to be monitored. Alternatively, for higher sensitivity, a Channel Electron Multiplier (CEM) can be used. This type of detector is a Secondary Electron Multiplier (SEM) in which a large negative potential ( ~2000 V) is used to attract the ions into the channel entrance. The channel is coated with a material that readily releases secondary electrons upon ion/electron impact. This produces a cascade of electrons down to the channel which can be detected, either as an electron current, or as a series of pulses.

TPD combined with a QMS is a sensitive technique, but it has several disadvantages: surface reaction products that remain in the solid phase cannot be probed *in situ*; additional surface reactions during the TPD (*i.e.*, during the linear heating of the ice and before complete desorption of the species) cannot be excluded; quantifying the desorbing species is not trivial as some of the interesting species have equal (*i.e.*, undistinguishable) masses and the analysis of the fractionated components of species upon electronic bombardment is not always straightforward. Finally, a TPD experiment inherently involves the destruction of the ice. Therefore, QMS data are mainly used here to constrain RAIRS data acquired during atom exposure of the ice.

### 2.2.3 Data analysis

After fitting the infrared spectra with connected straight baseline segments, the column densities (molecules $cm^{-2}$) of newly formed species can be determined from the integrated intensity of their infrared bands using a modified Lambert-Beer equation (Bennett *et al*. 2004):

$$N_X = \frac{\int A(\nu) d\nu}{S_X}, \qquad (2.1)$$

where A($\nu$) is the integrated absorbance and $S_X$ is the corresponding band strength. This equation can, however, only be used for thin ice layers. Teolis *et al*. (2007) showed that the proportionality between the optical depth and the ice abundance breaks down for thicker layers (~20 ML onwards); the integrated band area oscillates as a function of the layer thickness due to optical interference that is caused by the reflection at both the film-vacuum and film-substrate interfaces.

Since literature values of transmission band strengths cannot be used directly in reflectance measurements (Greenler 1966), an apparent absorption strength of stable species has to be calculated from calibration experiments. The determination of this apparent absorption strength is setup dependent. Therefore we performed a series of isothermal desorption experiments for the new apparatus introduced here to derive these values. Briefly, a layer of the selected ice is deposited at a temperature lower than its desorption temperature. The sample is then linearly heated to a temperature close to its desorption value. Infrared spectra are acquired regularly until the desorption of the ice is complete. The transition from zeroth-order to first-order desorption is assumed to occur at the onset to the submonolayer regime and appears in the desorption curve as a sudden change in slope (see Fig. 2.2). The apparent absorption strength in $cm^{-1}$ $ML^{-1}$ is then calculated by relating the observed integrated area to 1 ML in the modified Lambert-Beer

equation. We estimate the uncertainty of band strengths determined in this way to be large but within 50% (also see Fuchs *et al*. 2009, Ioppolo *et al*. 2011, Fraser *et al*. 2001).

The determination of the band strength allows for a quantitative study of stable species formed upon atom exposure of the ice. This is mostly the case in pre-deposited experiments. Isothermal desorption experiments of unstable intermediate species cannot be performed and therefore their band strengths cannot be derived. Thus, a qualitative study is generally performed in co-deposition experiments where unstable species are frozen in ice matrices and then detected in the infrared. In this case, formation trends of detected species are followed by integrating the corresponding band area as a function of time, *i.e.*, without calculating column densities. As a consequence, only formation trends of the same species obtained under different experimental conditions (*e.g.*, ice temperature, atom flux, ice composition) can be compared, but this still allows to derive valuable information on the involved reaction network.

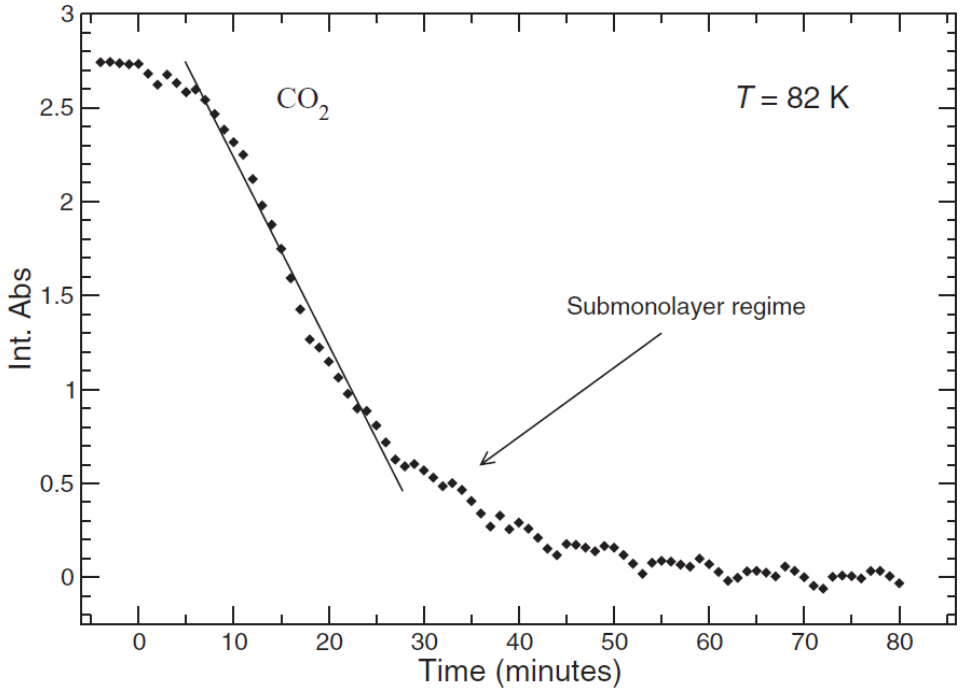


**Figure 2.2.** The decrease in integrated absorbance of $CO_2$ following desorption at a constant temperature of 82 K. The arrow indicates the transition point from the multi- to sub-monolayer regime.

### 2.2.4 Atom beam lines

Two different atom sources are used, one (HABS) based on thermal cracking, and the other (MWAS) using a microwave discharge (#9 and #13 in Fig. 2.1). The two custom-made

atom line chambers present identical geometrical characteristics (see Figs. 2.3 and 2.4): they are both pumped by 180 l/s (for $N_2$) turbomolecular pumps (Varian, TV 301 NAV); their room temperature base pressure is in the high $10^{-10}$ mbar regime (micro ion gauges, Granville-Phillips); they both are situated under an angle of 45° with respect to the substrate, both during single or simultaneous operation; a shutter is used to separate the lines from the main chamber; and a quartz pipe is placed after the shutter and along the path of the dissociated beam. The nose-shaped form of the pipe is designed to efficiently quench the excited electronic and ro-vibrational states of species through collisions with the walls of the pipe before they reach the ice sample. The geometry is designed in such a way that this is realized through at least four wall collisions of the atoms before leaving the pipe. In this way, “hot" species cannot reach the ice directly.

Two separate all metal dosing lines are used to prepare and inlet pure gasses and mixtures into each of the atom sources (#10 and #14 in Fig. 2.1). The dosing lines are pre-pumped with the same diaphragm pump that is used for evacuating the deposition dosing line. Each of the atom lines is then pumped with a 70 l/s (for $N_2$) turbomolecular pump (Pfeiffer Vacuum, TMU 071P). The room temperature base pressure of these lines is $< 1 \cdot 10^{-5}$ mbar and is monitored by means of a compact process ion gauge for each line (Pfeiffer Vacuum, IMR 265).

#### 2.2.4.1 HABS

An all metal precision leak valve is used to admit $H_2/D_2$ molecules (99.8% purity, Praxair) from the all metal dosing line into the capillary of a well characterized and commercially available thermal cracking source, a Hydrogen Atom Beam Source (HABS, Dr. Eberl MBE-Komponenten GmbH), see Tschersich & von Bonin (1998), Tschersich (2000), Tschersich *et al*. (2008), which is used to hydrogenate/deuterate the sample through heating the capillary from 300 to a maximum of 2250 K by a surrounding tungsten filament (see top-box in Fig. 2.3). During experiments the H + $H_2$ (D + $D_2$) flow through the capillary and the temperature of the tungsten filament are controlled and kept constant by adjusting the all metal valve position and the voltage of the power supply of the HABS (Delta Elektronika, SM 7020-D). The temperature of the filament is monitored by means of a C-type thermocouple placed close to the filament and inside the internal thermal shield. To prevent melting of components a water cooling system is implemented into the source, in thermal contact with an external copper thermal shield. The temperature of this shield is controlled with a second C-type thermocouple. The HABS is used in horizontal mode.

A wide range of atom beam fluxes is accessible with this source by changing the pressure in the capillary pipe and/or the temperature of the filament. Typically values cover a range from $10^{11}$ to $10^{13}$ atoms $cm^{-2}$ $s^{-1}$. Atom fluxes are measured at the sample position

in the main chamber, following a procedure described in section 2.2.5.1 (also see Bergh *et al*. 1999, Hidaka *et al*. 2004, Ioppolo *et al*. 2010).

As aforementioned, a quartz pipe is placed along the path of the beam (*i.e.*, after the shutter and before the sample in the main chamber) to cool the beam to room temperature. Previous experiments with liquid nitrogen cooled atom beams did not show any H/D-atom temperature dependence in CO hydrogenation reaction processes compared to experiments at room temperature (Watanabe & Kouchi 2002a). It is important to note that the relatively high temperature of 300 K of the incident H/D atoms in our experiments does not affect the experimental results, since H/D atoms are thermally adjusted to the surface temperature before they can react with other species through Langmuir-Hinshelwood mechanism, as shown in Fuchs *et al*. (2009), Hidaka *et al*. (2007), Watanabe *et al*. (2006).

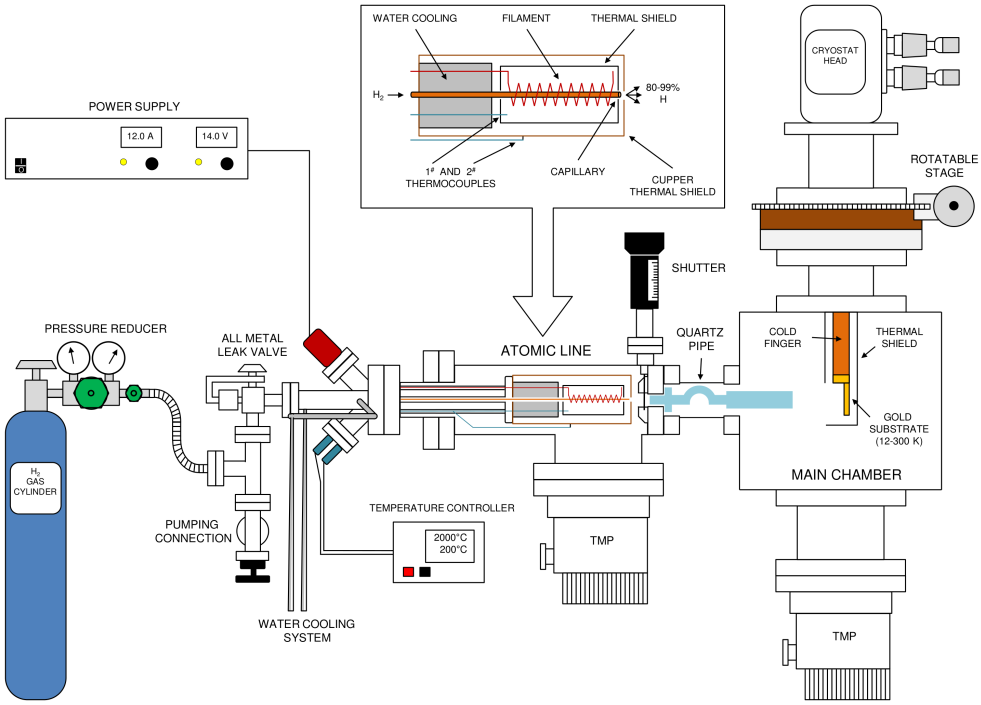


**Figure 2.3.** A schematic side-view of the atom line (HABS) with the thermal cracking H/D atom source and the main chamber

### 2.2.4.2 MWAS

A Microwave Atom Source (MWAS, Oxford Scientific Ltd) is included in the second atom line to produce beams of different atoms and radicals (*e.g.*, H, D, O, OH, OD, N). Figure

2.4 shows a schematic diagram of the MWAS. A 2.45 GHz microwave power supply (Sairem) produces up to 300 W that are coupled into a microwave cavity. Along this path a circulator is placed to avoid that the back-reflected power enters the power supply. A custom-made double tuner is placed after the circulator and before the microwave cavity to minimize the back-reflected power that ultimately is dissipated in a resistor. Part of the back-reflected signal is monitored by means of an oscilloscope (Tektronix, TDS 2012) connected to an attenuator and a crystal detector (Aertech Industries). An antenna (coaxial transmission line) connects the microwave cavity to a boron nitrite chamber in which gasses enter through the all metal precision leak valve of the dosing line (see top-box in Fig. 2.4). A plasma is created in a coaxial waveguide by coupling a radially symmetric 2.45 GHz microwave field to ions on the 86 mT surface of a multi-polar magnetic array (permanent magnets). The plasma is enhanced by the electron cyclotron resonance (ECR) effect. A water cooling system keeps the source and particularly the antenna close to room temperature. Moreover, the absence of a hot filament permits operation with most gases including reactive gases such as oxygen and nitrogen.

A specially designed alumina aperture plate allows reactive neutrals to escape from the plasma. The addition of an ion-trap (*i.e.*, two metal plates charged by a Oxford Scientific DC power supplier) can deflect the residual ion content from the beam, preventing ion exposure of the sample. All the electronically and ro-vibrationally excited species coming from the source are quenched through multiple collisions on passing through a quartz pipe before they reach the sample. Different plasma cavity pressures and/or different plasma power values give access to a wide range of atom fluxes, typically between $10^{10}$ and $10^{13}$ atoms $cm^{-2}$ $s^{-1}$. These numbers depend on the dissociated species (see next section).

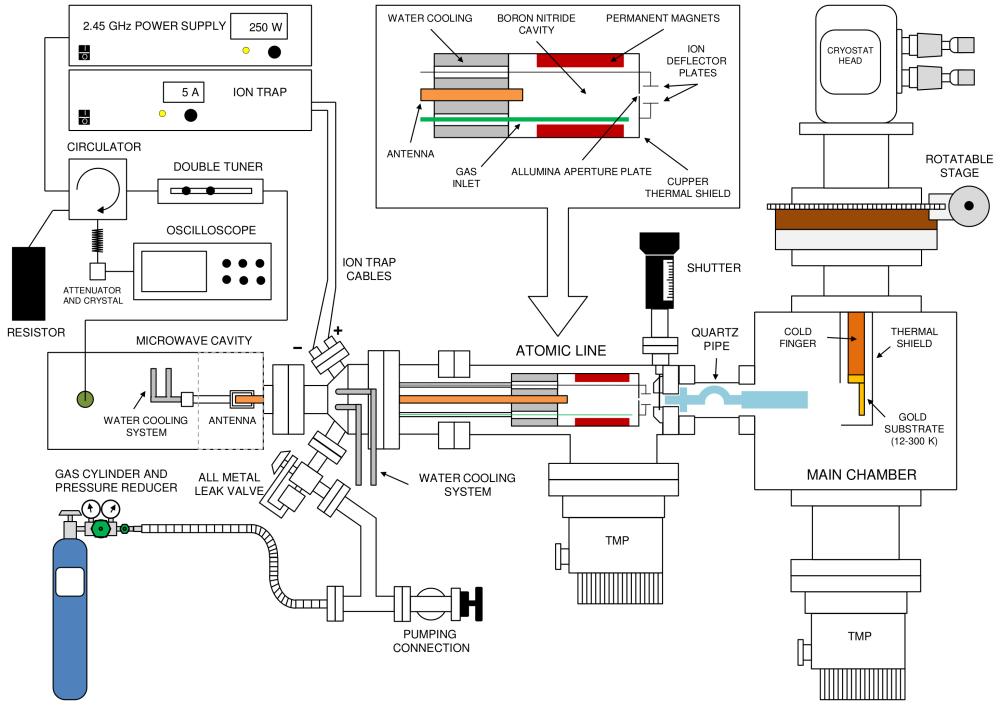


**Figure 2.4.** A schematic side-view of the atom line (MWAS) with the microwave plasma atom source and the main chamber.

### 2.2.5 Beam flux determinations

In order to measure the absolute D-atom fluxes for HABS and MWAS in the main chamber, the gold substrate is removed and the inlet of the QMS is placed at the center of the chamber facing the two atom lines, exactly at the same position and with the same angle that the substrate has when the ice is deposited and exposed to atom beam bombardment (see also Hidaka *et al*. 2007, Ioppolo *et al*. 2010). Since the sensitivity of the standard 1−200 amu QMS does not allow an accurate measurement at mass 1 amu, we measure the absolute D-atom fluxes instead of the H-atom fluxes for HABS and MWAS by following the aforementioned procedure. H-atom fluxes are then derived from the H/D ratio as obtained in selected experiments discussed in section 2.2.5.1.

The other MWAS absolute atom fluxes (*e.g.*, oxygen and nitrogen) cannot be measured mass spectrometrically because the background signal from the fractionated molecular species coming from the molecular component of the beam and the residual gas in the main chamber interferes with the signal coming straight from the atom beam. Therefore, effective O/N-atom fluxes are derived at the ice surface by using a new calibration method

described here for the first time and based on measuring the formation yield of final products of barrierless surface reactions (see sections 2.2.5.2 and 2.2.5.3).

### 2.2.5.1 H/D-atom beam fluxes

The D-atom and $D_2$ molecule fluxes for both HABS and MWAS are measured by monitoring masses 2 and 4 amu, respectively. Once the source is turned on, an increase in intensity of the D atoms is monitored with the QMS. The QMS measurements do not directly give the D-atom flux values. However, the increase in intensity of the QMS signal, $\Delta Q_D$, is proportional to the increase in pressure in the main chamber, $\Delta P_D$:

$$\Delta P_D = a \Delta Q_D. \qquad (2.2)$$

The setup specific proportionality factor a is measured from eq. (2.2) by introducing in the main chamber $D_2$ molecules instead of D atoms. The choice of $D_2$ is given by the fact that the factor a is independent of gas species, and that the D-atom beam contains a significant amount of undissociated $D_2$ molecules. Therefore, an exact measurement of $\Delta P_D$ is not trivial, while $\Delta P_{D_2}$ can be easily measured. The absolute D-atom fluxes are subsequently obtained from the following expression:

$$f_D = \frac{c_D \Delta P_D \langle v \rangle}{4 k_B T} = \frac{c_D a \Delta Q_D \langle v \rangle}{4 k_B T}, \qquad (2.3)$$

where cD is the calibration factor for the pressure gauge for D atoms taken from the specifications, $\langle v \rangle$ is the thermal velocity of the D atoms at 300 K, $k_B$ is the Boltzmann constant, and T is the D-atom temperature. Different D-atom fluxes are obtained by varying the filament temperature and/or the $D_2$ inlet flow with the HABS, and by changing the plasma cavity pressure and/or plasma power with the MWAS. Figure 2.5 shows the D-atom flux values produced by the HABS (left panel) and by the MWAS (right panel), as measured at the substrate site for different parameter settings. The relative error for D-atom fluxes (HABS and MWAS) is within 10%. The absolute error is within 50%. These errors may seem large, but it should be noticed that here atom fluxes at the ice surface are actually determined experimentally, whereas in previous studies these numbers are generally only estimated.

Since an absolute H-atom flux cannot be directly measured, the comparison between H- and D-atom fluxes is difficult. We compared the $H_2O_2$ and $D_2O_2$ formation rate upon $O_2$ hydrogenation and deuteration, which is flux dependent, in two identical 25 K experiments for both the HABS and the MWAS. The $H_2O_2$ formation rate was found to be a factor of

~2 higher than the $D_2O_2$ formation rate for both sources. This value confirms our previous finding in Ioppolo *et al*. (2010) and is used here to scale H-atom fluxes with an uncertainty of 50%. This simplistic way of measuring a scaling factor between H- and D-atom fluxes does not however take into account that H and D atoms can differ by (i) sticking probability onto the surface, (ii) hopping rate, (iii) $HO_2$ + H ($DO_2$ + D) branching ratio and reaction barrier, (iv) desorption probability, and (v) recombination probability with other H/D atoms. Therefore, a new method for the determination of the H-atom fluxes, based on trapping H and D atoms inside an $O_2$ ice matrix, is used in a future work to determine the effective H/D-atom fluxes at the ice surface. In brief, the reaction H + $O_2$ → $HO_2$ is barrierless under certain incoming angles in the gas phase. During co-deposition experiments, the angle dependence has a negligible physical importance since the oxygen beam provides $O_2$ molecules with a range of different orientations at the surface before they can align Lamberts *et al*. (2013). Therefore, the amount of $HO_2$ ($DO_2$) formed in the ice is proportional to the H- (D)-atom flux, and gives us an estimate of the effective fluxes at the cold surface. Preliminary results show that the trends found in Fig. 2.5 for the D-atom fluxes are reproduced for the H-atom fluxes as well, but an exact ratio between the H/D fluxes is still to be determined and will not be discussed here.

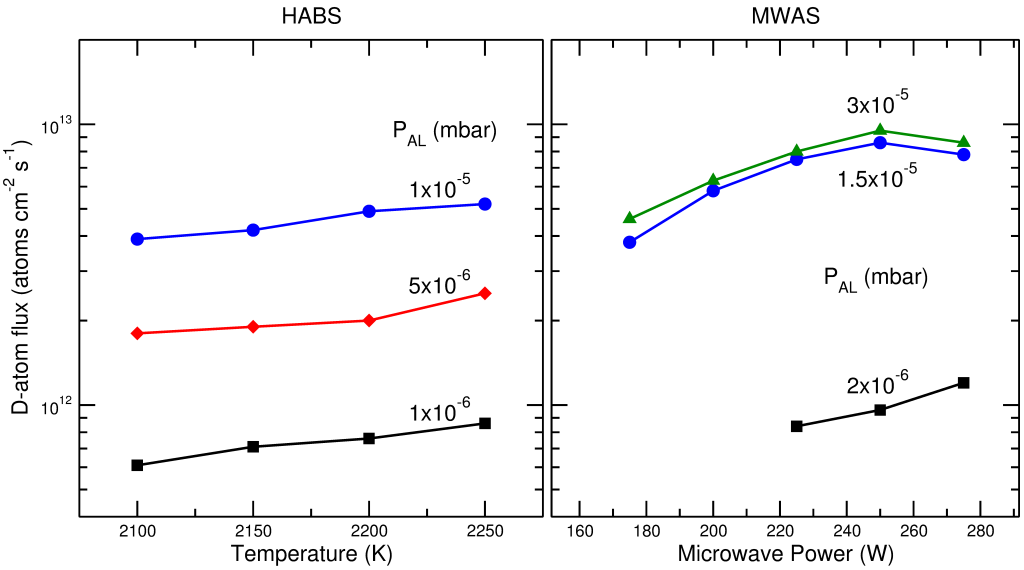


**Figure 2.5.** D-atom flux values as measured for the HABS (left panel) and the MWAS (right panel) at the substrate place for different parameter settings.

### 2.2.5.2 O-atom beam fluxes

The effective MWAS O-atom fluxes (*i.e.*, oxygen atoms directly involved in surface reactions) are derived by measuring the final column density of newly formed ozone ice after co-deposition of $^{16}O$ atoms and $^{18}O_2$ molecules at 15 K. The reaction $O_2 + O \rightarrow O_3$ is barrierless (Campbell & Gray 1973, Lin & Leu 1982), and therefore, we can safely assume that most of the oxygen atoms available for reaction on the surface will recombine to form ozone ice. Co-deposition experiments are used in order to avoid limitations in penetration depth of oxygen atoms into molecular oxygen ice.

Final fluxes are calculated from the knowledge of the duration of O-atom exposure, the number of monolayers of $O_3$ formed upon reaction, and assuming 1 ML = $10^{15}$ molecules $cm^{-2}$:

$$f_X = \frac{N_{X'} \times 10^{15}}{\text{exposure time}}, \qquad (4.4)$$

where $f_X$ is the O-atom flux, and $N_{X'} = N_{O_3} = {}^{16}O^{18}O^{18}O + {}^{16}O^{16}O^{16}O$ in monolayers. We do not count the $^{16}O_3$ contribution three times because solid $^{16}O_3$ is not likely to be formed through the sequential merging of $^{16}O$ atoms on the surface of the ice. Most of the $^{16}O_2$ can indeed form in the quartz pipe through recombination of $^{16}O$ atoms (see section 2.2.4.2), or it originates from a not fully dissociated beam, mainly in the case that $^{16}O$ atoms form through dissociation of $^{16}O_2$ gas molecules. The overall contribution of $^{16}O_2$ originating from the atom line is considerably smaller when $N_2O$ is used instead of $^{16}O_2$ as a precursor gas to produce $^{16}O$ atoms. This can be checked by comparing the amount of $^{16}O_3$ formed in the ice in co-deposition experiments of $^{16}O$ (from $^{16}O_2$) + $^{18}O_2$ at 15 K with the amount of $^{16}O_3$ formed in similar co-deposition experiments with $^{16}O$ from $N_2O$. Moreover, the amount of $^{16}O_3$ can be controlled by changing the ratio $^{16}O/^{18}O_2$. An over-abundance of $^{18}O_2$ minimizes the amount of $^{16}O_3$ formed in the ice because $^{16}O$ atoms react mostly with $^{18}O_2$. A negligible amount of $^{16}O_3$ in the co-deposition experiments gives $N_{O_3} \approx {}^{16}O^{18}O^{18}O$, and therefore a more direct and accurate O-atom flux value. This is true, especially when $^{16}O$ atoms are obtained from $N_2O$. Finally, the non-detection of the other ozone isotopologues (*e.g.*, $^{18}O^{16}O^{16}O$, $^{18}O^{16}O^{18}O$, or $^{18}O^{18}O^{18}O$) in our experiments indicates that isotopic exchange induced by surface destruction reactions, like $O_3 + O \rightarrow 2\ O_2$, is under the detection limit. Therefore, our method can be safely used to characterize the O-atom beam fluxes produced by the MWAS.

To quantify the amount of ozone produced in the oxygen flux-determination experiments, we derived the absorption band strength of ozone in two different ways: (i) performing an isothermal desorption experiment as described in section 2.2.3 (see left

panel of Fig. 2.6); (ii) measuring the consumption of ozone through hydrogenation reactions and assuming that hydrogen can penetrate only up to 2 ML of ozone ice. In the first case, in order to determine one monolayer of ozone, we first produce $^{16}O^{18}O^{18}O$ during 3 hrs of co-deposition of $^{16}O$ and $^{18}O_2$ at 35 K. Subsequently, an isothermal desorption experiment is performed at 58.5 K. From the offset between zeroth-order and first-order desorption we estimate the band strength of $^{16}O^{18}O^{18}O$. In the second case, a co-deposition of $^{16}O$ and $^{18}O_2$ at 15 K is performed for 3 hrs to form again $^{16}O^{18}O^{18}O$. The ice is then annealed to 50 K in order to remove the molecular oxygen and to realize a pure ozone ice. The $^{16}O^{18}O^{18}O$ ice is then exposed to H atoms at 15 K to monitor the destruction of the ozone layer. Assuming that only ~2 ML of ozone ice are fully hydrogenated, Romanzin *et al*. 2011 derive the number of ozone molecules destroyed upon hydrogenation per monolayer, which gives us back the apparent band strength for $^{16}O^{18}O^{18}O$. The final band strength for ozone is confirmed within 30% of uncertainty by the two different methods.

To verify that 1 ML of ozone is destroyed by 1 ML of H or D atoms (following reaction $O_3$ + H/D → $O_2$ + OH/OD), and that our calibration methods used here to determine the D/H/O/N atom fluxes lead to coherent results, we performed a control experiment. A new co-deposition of $^{16}O$ and $^{18}O_2$ at 35 K is performed for 40 minutes to form ~2 ML of $^{16}O^{18}O^{18}O$ ice. The ice is then heated up to 50 K in order to have a layer of pure ozone ice. The $^{16}O^{18}O^{18}O$ ice is then exposed to D atoms at the same temperature to monitor the destruction of the ozone layer versus the time of exposure. We use D atoms instead of H atoms, because the deuterium flux is more accurately determined, as described before. Moreover, at 50 K secondary reaction products, like $O_2$, will desorb without reacting with D atoms and therefore leaving mainly $O_3$ on the surface to be processed. The right panel of Fig. 2.6 shows three infrared spectra of ozone ice at different thickness in the range of the $\nu_3$ mode (see Table 2.2). These spectra are acquired during the deuteration of the ~2 ML of $^{16}O^{18}O^{18}O$ ice. The central panel of Fig. 2.6 shows the integrated absorbance of $^{16}O^{18}O^{18}O$ versus the D-atom fluence. The left panel shows the aforementioned isothermal desorption experiment of $O_3$ ice at 58.5 K used to identify the integrated absorbance of solid $O_3$ that corresponds to 1 ML of thickness. From the knowledge of the ozone apparent band strength and the data shown in the central panel of Fig. 2.6, we derive that 1 ML of $O_3$ is consumed by ~1.5 ML of D atoms, which is within the experimental uncertainties of apparent band strength and D-atom flux determination.

The $^{16}O_3$ apparent band strength is obtained from the available data for $^{16}O^{18}O^{18}O$ for our setup and the ratio between the transmission band strengths for $^{16}O_3$ and $^{16}O^{18}O^{18}O$ (for the transmission band strength values see Sivaraman *et al*. (2011). According to eq. 4 standard O-atom fluxes span in the range between $10^{11}$ and $10^{12}$ atoms $cm^{-2}$ $s^{-1}$. The O-atom flux values shown in Table 2.1 have to be considered as lower limits because (i) fluxes are derived indirectly (effective fluxes), (ii) some of the $^{16}O$ can recombine on the

surface of the ice, and (iii) $^{16}O_2$ can potentially not be further oxygenated to form ozone because it is trapped into the $^{18}O_2$ matrix. The dissociation rates shown in Table 1 are obtained by comparing the undissociated molecular component of the beam (*i.e.*, $N_2O$, $O_2$, $N_2$) measured mass spectrometrically (*i.e.*, with the atom source on and the QMS placed at the center of the main chamber) with the O- and N-atom flux values as derived in sections 2.2.5.2 and 2.2.5.3, respectively.

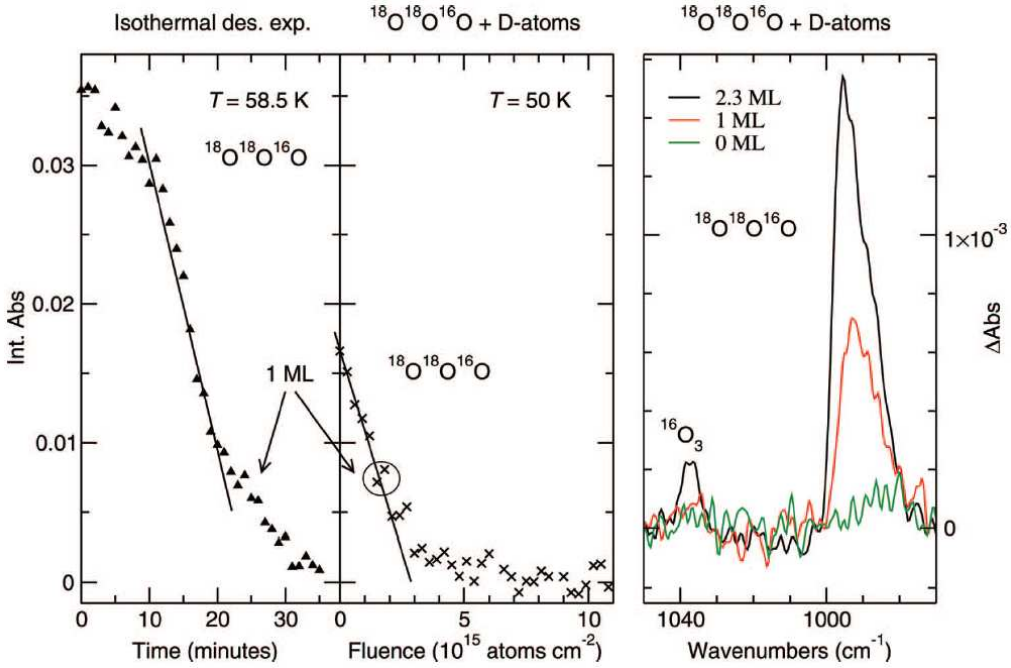


**Figure 2.6.** The left panel shows the isothermal desorption experiment of $O_3$ ice at 58.5 K. The central pannel shows the destruction of ~2 ML thick $O_3$ ice versus the D-atom fluence at 50 K. In both left and center panel, the lines and the circle are used to guide the eye. The right panel shows selected infrared spectra of ozone deuteration at 50 K for different ice thicknesses in the spectral range of the $\nu_3$ mode.

### 2.2.5.3 N-atom beam fluxes

As for the MWAS O-atom fluxes, the determination of effective nitrogen-atom fluxes is obtained indirectly by measuring the final column density of newly formed dinitrogen trioxide ($N_2O_3$) ice after co-deposition of $^{15}N$ atoms and NO molecules at 15 K. In this particular experiment, a sequence of barrierless (or very low barrier) surface reactions is involved in the formation of $N_2O_3$ (Campbell & Gray 1973, Schieferstein *et al*. 1983, Markwalder *et al*. 1993): N + NO → $N_2$ + O, NO + O → $NO_2$, and $NO_2$ + NO → $N_2O_3$. Therefore in this specific case, N-atom fluxes are directly proportional to the amount of

$N_2O_3$ formed in the ice, and are determined by using eq. (2.4), where $f_X$ is the N-atom flux, and $N_{X'} = N_{N_2O_3}$ which is the amount of monolayers of $N_2O_3$ formed in the ice after a certain time of N-atom exposure.

As in section 2.2.5.2, we use two different methods to obtain the apparent $N_2O_3$ band strength. In particular, two new co-deposition experiments of NO and $O_2$ are performed at 15 K. Also in this case $N_2O_3$ is formed through surface reactions. The ice obtained from these two experiments is in both cases heated up to remove the NO trapped in the ice. In one of the two experiments, the ice temperature is then kept at 121 K to monitor the desorption of $N_2O_3$ (isothermal desorption experiment). From this experiment we obtain the band strength for $N_2O_3$, as discussed in the latter sections. In the second experiment, the ice is cooled down again to 15 K and subsequently hydrogenated to see the destruction of $N_2O_3$. The penetration depth of hydrogen into $N_2O_3$ ice is expected to involve only a few monolayers, as for $O_3$, CO, and NO ice (Romanzin *et al*. 2011, Fuchs *et al*. 2009, Fedoseev *et al*. 2012). Therefore, assuming that only ~2 ML of $N_2O_3$ are consumed by the surface hydrogenation of the ice, we can estimate the band strength of $N_2O_3$ which is found to be consistent with the value obtained from the isothermal desorption experiment within 40% of uncertainty.

The N-atom flux values are roughly one order of magnitude lower than the O-atom values (see Table 2.1). As explained in section 2.5.2, these values are all lower limits, because of the way the fluxes are derived. In the specific case of nitrogen fluxes, the formation of $N_2O_3$ is a three step reaction, and therefore the single reactant can further react with the others to form $N_2O_3$, or alternatively desorb, or be trapped in a NO matrix. Therefore, we expect the O- and N-atom absolute fluxes to be higher than reported in Table 2.1.

**Table 2.1.** The effective O- and N-atom fluxes as derived from the formation yields of solid species in the ice upon barrierless reactions (see eq. 4.4).

| Effective atom flux | High (atoms $cm^{-2}$ $s^{-1}$) | Dissociation rate (%) | Low (atoms $cm^{-2}$ $s^{-1}$) | Dissociation rate (%) |
|---|---|---|---|---|
| $^{16}O$ from $O_2$ | $9 \cdot 10^{11}$ | 8 | $2 \cdot 10^{11}$ | 12 |
| $^{16}O$ from $N_2O$ | $7 \cdot 10^{11}$ | 19 | $1 \cdot 10^{11}$ | 10 |
| $^{15}N$ from $^{15}N_2$ | $9 \cdot 10^{10}$ | 0.4 | — | — |
| $^{14}N$ from $^{14}N_2$ | $8 \cdot 10^{10}$ | 0.4 | — | — |

## 2.3 Experimental results

In this section we present the first science results obtained with SURFRESIDE$^2$ in order to demonstrate its performance and to illustrate the potential of the experimental setup. Figure

2.7 shows the IR spectrum of $^{13}CO$ co-deposited with oxygen and hydrogen atoms on a 13.5 K gold substrate ($^{13}CO$ + O + H). This spectrum is compared to co-deposition spectra of $^{13}CO$ and oxygen atoms ($^{13}CO$ + O); $^{13}CO$ and hydrogen atoms ($^{13}CO$ + H); and oxygen atoms and hydrogen atoms (O + H). In all four experiments, oxygen atoms are produced by the MWAS, while hydrogen atoms are formed by the HABS. The $^{13}CO$ deposition rate (0.0075 ML $s^{-1}$) as well as O- and H-atom fluxes ($1 \cdot 10^{11}$ and $1 \cdot 10^{13}$ atoms $cm^{-2}$ $s^{-1}$, respectively) are kept the same in all the experiments and the spectra shown in Fig. 2.7 are all acquired after 45 minutes of co-deposition. As discussed in section 2.2.5, the O-atom flux value is an effective flux at the ice surface, while the H-atom flux is scaled from the absolute D-atom flux value which is probably higher than the effective flux at the cold surface. Therefore for instance, the H/O ratio presented below has to be considered as an upper limit for H atoms. Oxygen atoms are obtained by dissociating $N_2O$ in the microwave atom source. This explains the presence of nitrogen-bearing species in the ice when the O-atom beam line is used (see Fig. 2.7 and Table 2.2).

The aforementioned experiments demonstrate the advantage of having a double atom beam line when investigating surface atom addition reactions. The choice of using one or both atom lines allows us to select, investigate, compare, and combine different reaction channels. For instance, in order to better interpret results from the simultaneous hydrogenation and oxygenation of solid CO, it is necessary to first distinguish the single contributions of the different reaction channels, *i.e.*, O + H, CO + H, and CO + O:

- The O + H spectrum in Fig. 2.7 shows the presence of $N_2O$ from the not fully ($N_2O$) dissociated O-atom beam. The amount of water formed in this experiment is around the detection limit, while $H_2O_2$ is below the detection limit. The limiting factor on the production of water ice is the number of O atoms available to react with the H atoms on the cold surface (H/O ~ 100). After 45 minutes of co-addition of O and H atoms, only 0.2 ML of water can be formed assuming that all the oxygen available will react to form water. Surface formation of water ice through the hydrogenation of $O/O_2/O_3$ has been the object of many recent physical-chemical and astrochemical relevant studies (Dulieu *et al*. 2010, Miyauchi *et al*. 2008, Ioppolo *et al*. 2008, Matar *et al*. 2008, Ioppolo *et al*. 2010, Cuppen *et al*. 2010, Lamberts *et al*. 2013, Mokrane *et al*. 2009, Romanzin *et al*. 2011) and is not extensively discussed in this paper again.
- Formaldehyde is clearly present in the $^{13}CO$ + H spectrum (Fig. 2.7), whereas methanol is not. As previously shown Watanabe & Kouchi (2002a), Fuchs *et al*. (2009), formaldehyde and methanol are the main final products of solid CO hydrogenation. However, methanol is under the detection limit in the experiment shown in Fig. 2.7 because of the low penetration depth ( ~ 4 ML) of hydrogen atoms into a CO ice Fuchs *et al*. (2009), as well as a comparable abundance of CO with respect to hydrogen atoms (CO/H ~ 0.75). The amount of hydrogen atoms available to react with CO molecules is

further lowered by the molecular hydrogen recombination on the surface. Therefore, the newly formed $H_2CO$ ice is not further hydrogenated under these experimental conditions. For other conditions (see Fuchs *et al*. 2009) it does.

- The $^{13}CO$ + O spectrum in Fig. 2.7 is the richest in absorption features due to N-bearing molecules, like $N_2O$, $NO_2$, $N_2O_3$, $(NO)_2$ dimer, and NO monomer. These species are either coming from the not fully dissociated O-atom beam or are formed through surface oxygenation of other N-bearing species. Alternatively, O atoms recombine in the ice with each other to form $O_2$ and $O_3$, or react with CO to form carbon dioxide.
- The surface reaction products present in the $^{13}CO$ + O + H spectrum (Fig. 2.7) come from the single isolated aforementioned reaction routes as well as from the interaction of different reaction products with each other. Ozone, methanol, and hydrogen peroxide are under the detection limit, while water ice is slightly above it. Formaldehyde and mostly carbon dioxide are visible in the spectrum. The only nitrogen-bearing species clearly present in the ice is $N_2O$. In the $^{13}CO$ + O + H experiment the final column density of solid $^{13}CO_2$ is ten times higher than in the case of the $^{13}CO$ + O experiment (see inset in Fig. 2.7).

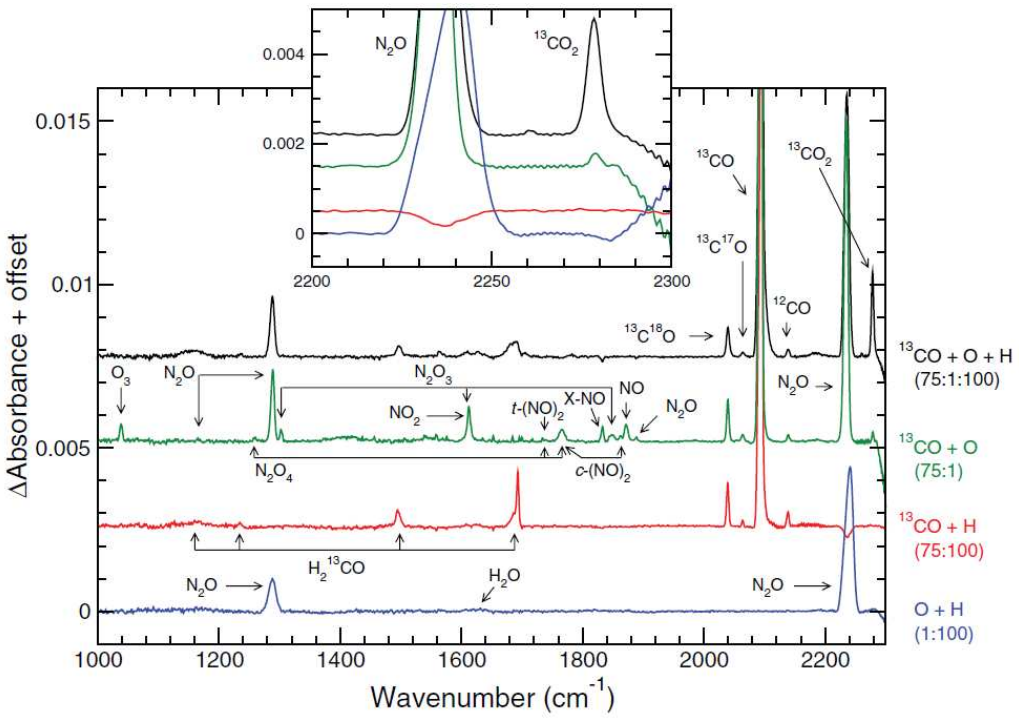


**Figure 2.7.** RAIR co-deposition spectra of $^{13}CO$, O- and H-atoms on a 13.5 K gold substrate (top-spectrum in main panel, $^{13}CO$ + O + H); $^{13}CO$ and O-atoms (second spectrum from the top, $^{13}CO$ + O); $^{13}CO$ and H-atoms (third spectrum from the top, $^{13}CO$ + H); and O- and H-atoms (bottom-spectrum, O + H). The inset figure shows the $^{13}CO_2$ stretching mode region for all four experiments.

The focus of the following section is on the formation of solid carbon dioxide at low temperatures through surface reactions induced by non-energetic processing. The chemical origin of solid $CO_2$ as observed in our experiments is subsequently discussed and placed in an astronomical context.

**Table 2.2.** Assigned infrared features with their corresponding references.

| Position, $cm^{-1}$ | Species | Mode | Reference |
|---|---|---|---|
| 1040 | $O_3$ | $\nu_3$ | Brosset *et al*. (1993), Chaabouni *et al*. (2000), Bennett & Kaiser (2005) |
| 1162 | $H_2{}^{13}CO$ | $\nu_4$ | Wohar & Jagodzinski (1991) |
| 1167 | $N_2O$ | $2\nu_2$ | Dows (1957), Łapiński *et al*. (2001) |
| 1240 | $H_2{}^{13}CO$ | $\nu_6$ | Wohar & Jagodzinski (1991) |
| 1260 | $N_2O_4$ | $\nu_{11}$ | Holland & Maier II (1983) |
| 1289 | $N_2O$ | $\nu_1$ | Jamieson *et al*. (2005), Dows (1957), Łapiński *et al*. (2001) |
| 1304 | $N_2O_3$ | $\nu_3$ | Fateley *et al*. (1959), Nour *et al*. (1983) |
| 1497 | $H_2{}^{13}CO$ | $\nu_3$ | Wohar & Jagodzinski (1991) |
| 1612 | $NO_2/N_2O_3$ | $\nu_3/\nu_2$ | Fateley *et al*. (1959), Jamieson *et al*. (2005) / Fateley *et al*. (1959), Nour *et al*. (1983) |
| 1630 | $H_2O$ | $\nu_2$ | Hagen & Tielens (1981) |
| 1694 | $H_2{}^{13}CO$ | $\nu_2$ | Wohar & Jagodzinski (1991) |
| 1737 | $t$-$(NO)_2/N_2O_4$ | $\nu_1/\nu_9$ | Fateley *et al*. (1959) / Holland & Maier II (1983) |
| 1766 | $c$-$(NO)_2/N_2O_4$ | $\nu_5/\nu_9$ | Fateley *et al*. (1959), Nour et. al. (1984) / Holland & Maier II (1983) |
| 1833 | X-NO | | Fedoseev *et al*. (2012) |
| 1850 | $N_2O_3$ | $\nu_1$ | Fateley *et al*. (1959), Nour *et al*. (1983) |
| 1864 | $c$-$(NO)_2$ | $\nu_1$ | Fateley *et al*. (1959), Nour *et al*. (1984) |
| 1872 | NO (monomer) | $\nu_1$ | Fateley *et al*. (1959), Nour *et al*. (1984), Holland & Maier II (1983) |
| 1888 | $N_2O$ | $\nu_1+\nu_2$ | Dows (1957), Łapiński *et al*. (2001) |
| 2039 | $^{13}C^{18}O$ | $\nu_1$ | Loeffler *et al*. (2005) |
| 2066 | $^{13}C^{17}O$ | $\nu_1$ | Loeffler *et al*. (2005) |
| 2096 | $^{13}CO$ | $\nu_1$ | Ewing & Pimentel (1961) |
| 2139 | CO | $\nu_1$ | Sandford *et al*. (1988) |
| 2235 | $N_2O$ | $\nu_3$ | Dows (1957), Łapiński *et al*. (2001), Jamieson *et al*. (2005) |
| 2278 | $^{13}CO_2$ | $\nu_3$ | Berney & Eggers (1964) |

### 2.3.1 Astrochemical implications

It is generally accepted that due to its low gas-phase abundance ($CO_2^{gas}/CO_2^{ice} \ll 1$) carbon dioxide is formed in the solid phase in the interstellar medium on the surface of icy dust grains (10−20 K) through surface reactions involving energetic (*e.g.*, UV photolysis, cosmic rays irradiation, thermal processing) and non-energetic processing (*e.g.*, atom bombardment), see van Dishoeck *et al*. (1996), Boonman *et al*. (2003). Solid CO is the $CO_2$ precursor that has been mostly studied in literature. The most cited surface reaction routes involving solid CO are:

$$CO + O \rightarrow CO_2, \quad (2.5)$$
$$HCO + O \rightarrow CO_2 + H, \quad (2.6)$$
$$CO + OH \rightarrow CO_2 + H. \quad (2.7)$$

These reaction routes can be activated by both energetic and non-energetic processing. For instance, solid $CO_2$ can form from the interaction of energetic photons/ions and pure CO molecules or CO-bearing mixtures (Garozzo *et al*. 2011, Ioppolo *et al*. 2013, Moore *et al*. 1991, Gerakines *et al*. 1996, Ehrenfreund *et al*. 1997, Palumbo *et al*. 1998, Satorre *et al*. 2000, Watanabe *et al*. 2002b, Loeffler *et al*. 2005, Ioppolo *et al*. 2009). Solid $CO_2$ can, however, also be formed through photolysis/radiolysis of amorphous carbon capped with a layer of water or oxygen ice (Mennella *et al*. 2004, Mennella *et al*. 2006, Gomis & Strazzulla 2005, Raut *et al*. 2012, Fulvio *et al*. 2012).

In space, thermal atom-addition induced chemistry is more dominant in quiescent cold interstellar regions, where newly formed species are protected from radiation to a great extent by dust particles. In these regions, solid $CO_2$ can form through reactions (2.5)-(2.7). Reaction (2.5) has been investigated experimentally in Roser *et al*. (2001), Madzunkov *et al*. (2006), Raut *et al*. (2012). Raut & Baragiola (2011) showed that $CO_2$ forms in small quantities during co-deposition of CO and cooled O atoms and $O_2$ molecules into thin films at 20 K. The reason for the low $CO_2$ yield is that O atoms react preferentialy with O to form $O_2$, and with $O_2$ to form $O_3$. The latter experimental findings, also supported by theoretical studies (Talbi *et al*. 2006), indicate that the surface reaction (2.5) has a barrier of ~2000 K in the gas phase (Slanger *et al*. 1972). Moreover, Goumans & Andersson (2010) showed that although tunnelling increases the surface reaction rate for reaction $O(^3P) + CO$ at low temperatures, the onset of tunnelling is at too low temperatures for the reaction to significantly contribute to the formation of solid $CO_2$ under interstellar conditions. Therefore, reaction (2.5) is not an efficient $CO_2$ formation pathway unless energetic processing is involved. Our laboratory results from the CO + O experiment (Fig. 2.7) show

indeed a more efficient production of ozone compared to carbon dioxide at 13.5 K, and are consistent with previous findings.

Solid $CO_2$ can also form through reaction (2.6) (Ruffle & Herbst 2001), which is experimentally challenging to investigate in the solid phase because other $CO_2$ formation reaction routes will compete. Moreover, when the H/O ratio is in favor of H atoms, the hydrogenation of CO ice will convert most of the HCO in formaldehyde and methanol. Therefore, this route is negligible under our experimental conditions, and we will further not consider it in our discussion.

Alternatively, solid $CO_2$ can be formed through reaction (2.7), which yields a HOCO intermediate. This complex can directly dissociate, forming solid $CO_2$ and leaving a H atom, or can be stabilized by intramolecular energy transfer to the ice surface and eventually react with an incoming H atom in a barrierless manner to form $CO_2$ and $H_2$ or other products with a purely statistical branching ratio as theoretically shown by Goumans *et al.* (2008). Recently, several independent experimental studies showed that reaction (2.7) is an efficient surface $CO_2$ formation channel without need for an energetic input (Oba *et al.* 2010a, Ioppolo *et al.* 2011a, Noble *et al.* 2011. In earlier work (Ioppolo *et al.* 2011a), we demonstrated with a one beam line system the formation of $CO_2$ at low temperatures through reaction (2.7) by hydrogenation of a $CO{:}O_2$ binary ice mixture. In that case, we used a single H-atom beam line. Here, we are able to compare reactions (2.5) and (2.7) under the same experimental conditions by using two atom beam lines.

Reactions (2.5)-(2.7) have never been experimentally compared with each other before under the same laboratory conditions. So far, only theoretical work investigated these surface reactions within a larger astrochemical reaction network. For instance, Garrod & Pauly (2011) studied in their three-phase (gas/surface/mantle) astrochemical model the formation and evolution of interstellar dust-grain ices under dark-cloud conditions, with a particular emphasis on $CO_2$. By including reactions (2.5)-(2.7) in their reaction network, they were able to reproduce the observed behavior of $CO_2$, CO, and water ice in the interstellar medium. Furthermore, reaction (2.7) was found to be efficient enough to account for the observed $CO_2$ ice production in dark clouds.

Our experimental results confirm the conclusions found in Garrod & Pauly (2011). The $^{13}CO_2$ formed in the $^{13}CO + O + H$ experiment is ten times more abundant than the $^{13}CO_2$ formed in the $^{13}CO + O$ experiment. In the $^{13}CO + O + H$ experiment, solid $^{13}CO_2$ is mainly formed through the HOCO intermediate. Under these experimental conditions, all the O atoms will indeed react in a barrierless way with H atoms to form hydroxyl radicals that will either react with another H atom to form $H_2O$, or will react with $^{13}CO$ to form $^{13}CO_2$. The non-detection of ozone and other N-bearing products formed in the ice is due to the overabundance of H atoms, and confirms that O atoms are all used-up to form OH radicals. Moreover, the presence of formaldehyde in the ice indicates that H atoms are over

abundant with respect to O atoms. Solid HCOOH and $H_2CO_3$ are under the detection limit. The non-detection of these two species that are formed through the hydrogenation of the HOCO complex and the reaction of the latter with the hydroxyl radical, respectively, Ioppolo *et al*. (2011b) and Oba *et al*. (2010b) indicate that the HOCO complex is efficiently dissociated in $CO_2$ + H under our experimental conditions.

The fact that the $^{13}CO_2$ formed in the $^{13}CO$ + O + H experiment is ten times more abundant than the $^{13}CO_2$ formed in the $^{13}CO$ + O experiment indicates that reaction (2.7) has a lower activation barrier and is faster than reaction (2.5). Chang & Herbst (2012) investigated the surface reaction CO + O + H among others by means of a unified microscopic-macroscopic Monte Carlo simulation of gas-grain chemistry in cold interstellar clouds in which both the gas-phase and the grain-surface chemistry are simulated by a stochastic technique. In their model, solid $CO_2$ is produced mainly by reaction (2.7), which occurs by a so-called “chain reaction mechanism", in which an H atom first combines with an O atom lying above a CO molecule, so that the OH does not need to undergo horizontal diffusion to react with CO. Their $CO_2$ calculated abundances are in good agreement with observations (Oberg *et al*. 2011). Moreover, this scenario is not far from our experimental conditions, where O and H atoms meet to form OH radicals that then further react with neighboring CO molecules to form $CO_2$. This shows that SURFRESIDE[2] is suited to investigate astrochemical relevant surface reaction networks. Chang & Herbst (2012) finally suggested that the solid CO formed in early cold cloud stages via accretion and surface reactions is mainly converted into $CO_2$ through reaction (2.7). This makes reaction (2.7) to be most likely the main non-energetic $CO_2$ formation route under early cold cloud conditions, where H atoms are orders of magnitude more abundant than O atoms (Dupuis *et al*. 2009). Chang & Herbst (2012) also suggested that the conversion of CO into $CO_2$ becomes inefficient at later times, where, for the low-mass YSO case, there can be a high abundance of almost pure CO, with some conversion to formaldehyde and methanol. Under these conditions, solid $CO_2$ can still be formed via energetic processing (Ioppolo *et al*. 2013).

### 2.4 Conclusions

We have presented a novel and versatile UHV setup designed for the quantitative investigation of interstellar relevant surface processes under fully controlled conditions. The system implements a main chamber and two atom beam lines. Molecules are deposited in the main chamber onto a cold gold substrate, able to reproduce interstellar dense cloud temperatures and ice thicknesses. The ice is monitored with a FTIR spectrometer, while gas phase species present in the chamber are monitored with a QMS. As for interstellar ices in dense cloud conditions, laboratory ices are exposed to (H/D/O/N) atom beam fluxes. These

are accurately determined using a chemical calibration procedure. The choice of using one or both atom lines sequentially or at the same time allows us to characterize interstellar relevant reaction channels in a bottom-up approach. In particular, the design of the system is suited for the isolation of single surface reaction channels and the comparison of their efficiency with those of other surface reactions that lead to the same final products. Here we demonstrate the potential of the system by studying the efficiency of solid $CO_2$ formation through surface reactions induced by atom addition. We find that under the same experimental conditions $CO_2$ is formed through the reaction CO + OH more efficiently than through the reaction CO + O. Our results are in good agreement with the most recent astrochemical models and observations (Chang & Herbst 2012, Oberg *et al*. 2011), and therefore show that SURFRESIDE$^2$ has the potential to solve important questions within the field of astrochemistry.

The results that we present here illustrate only one of the possible applications of SURFRESIDE$^2$. This system will indeed shine light on several other unresolved topics in astrochemistry, such as the competition between hydrogenation and deuteration of interstellar relevant species linking planetary H/D abundances to interstellar processes. SURFRESIDE$^2$ is ultimately designed to study the surface formation of complex organic molecules (COMs), sugars, and amino-acids under interstellar relevant conditions by sequential or co-addition of the different reactive components of those species onto the cold substrate. The use of a double beam line system is essential to achieve this aim. The future implementation of these and similar experimental results into astrochemical models that take into account astronomical fluxes and timescales as well as energetic and non-energetic processes is needed to understand the pathways that lead to molecular complexity in space.

**References**


Acharyya K., Fuchs G. W., Fraser H. J., van Dishoeck E. F., Linnartz H., 2007, A&A, 466, 1005

Bennett C. J., Jamieson C., Mebel A. M., Kaiser R. I., 2004, PCCP, 6, 735

Bennett C. J., Kaiser R. I., 2005, ApJ, 635, 1362

Bergh H. S., Gergen B., Nienhaus H., Majumdar A., Weinberg W. H., McFarland E. W., 1999, Rev. Sci. Instrum., 70, 2087

Berney C. V., Eggers D. F., Jr., 1964, JCP, 40, 990

Bisschop S. E., Fuchs G. W., van Dishoeck E. F., Linnartz H., 2007, A&A, 474, 1061

Blagojevic V., Petrie S., Bohme D. K., 2003, MNRAS, 339, L7

Boonman A. M. S., van Dishoeck E. F., Lahuis F., Doty S. D., 2003, A&A, 399, 1063

Brosset P., Dahoo R., Gauthierroy B., Abouafmarguin L., Lakhlifi A., 1993, Chem. Phys., 172, 315

Campbell I. M., Gray C. N., 1973, Chem. Phys. Lett., 18, 607

Chaabouni H., Schriver-Mazzuoli L., Schriver A., 2000, Low Temp. Phys., 26, 712

Chang Q., Herbst E., 2012, ApJ, 759, 147

Congiu E. *et al*., 2012a, ApJL, 750, L12

Congiu E., Chaabouni H., Laffon C., Parent P., Baouche S., Dulieu F., 2012b, JCP, 137, 054713

Cuppen H. M., Ioppolo S., Romanzin C., Linnartz H., 2010, PCCP, 12, 12077

Dows D. A., 1957, JCP, 26, 745

Dulieu F., Amiaud L., Congiu E., Fillion J., Matar E., Momeni A., Pirronello V., Lemaire J. L., 2010, A&A, 512, A30

Dupuis J., Oliveira C. M., Hebrard G. H., Moos H. W., Sonnentrucker P., 2009, ApJ, 690, 1045

Ehrenfreund P., Boogert A. C. A., Gerakines P. A., Tielens A. G. G. M., van Dishoeck E. F., 1997, A&A, 328, 649

Ewing G. E., Pimentel G. C., 1961, JCP, 35, 925

Fateley W. G., Bent H. A., Crawford B., Jr., 1959, JCP, 31, 204

Fedoseev G., Ioppolo S., Lamberts T., Zhen J. F., Cuppen H. M., Linnartz H., 2012, JCP, 137, 054714

Fraser H. J., Collings M. P., McCoustra M. R. S., Williams D. A., 2001, MNRAS, 327, 1165

Fuchs G.W., Cuppen H. M., Ioppolo S., Bisschop S. E., Andersson S., van Dishoeck E. F., Linnartz H., 2009, A&A, 505, 629

Fulvio D., Raut U., Baragiola R. A., 2012, ApJL, 752, L33

Garozzo M., La Rosa L., Kanuchova Z., Ioppolo S., Baratta G. A., Palumbo M. E., Strazzulla G., 2011, A&A, 528, 118

Garrod R. T., Pauly T., 2011, ApJ, 735, 15

Gerakines P. A., Schutte W. A., Ehrenfreund P., 1996, A&A, 312, 289

Gomis O., Strazzulla G., 2005, Icarus, 177, 570

Goumans T. P. M., Andersson S., 2010, MNRAS, 406, 2213

Goumans T. P. M., Uppal M. A., Brown W. A., 2008, MNRAS, 384, 1158

Greenler R. G., 1966, JCP, 44, 310

Hagen W., Tielens A. G. G. M., JCP, 75, 4198

Hidaka H., Kouchi A., Watanabe N., 2007, JCP, 126, 204707

Hidaka H., Watanabe N., Shiraki T., Nagaoka A., Kouchi A., 2004, ApJ, 614, 1124

Hiraoka K., Ohashi N., Kihara Y., Yamamoto K., Sato T., Yamashita A., 1994, Chem. Phys. Lett., 229, 408

Holland R. F., Maier II W. B., 1983, JCP, 78, 2928

Ioppolo S., Cuppen H. M., Romanzin C., van Dishoeck E. F., Linnartz H., 2008, ApJ, 686, 1474

Ioppolo S., Cuppen H. M., Romanzin C., van Dishoeck E. F., Linnartz H., 2010, PCCP, 12, 12065

Ioppolo S., Cuppen H. M., van Dishoeck E. F., Linnartz H., 2011b, MNRAS, 410, 1089

Ioppolo S., Palumbo M. E., Baratta G. A., Mennella V., 2009, A&A, 493, 1017

Ioppolo S., Sangiorgio I., Baratta G. A., Palumbo M. E., 2013, A&A, 554, A34

Ioppolo S., van Boheemen Y., Cuppen H. M., van Dishoeck E. F., Linnartz H., 2011a, MNRAS, 413, 2281

Jamieson C. S., Bennett C. J., Mebel A. M., Kaiser R. I., 2005, ApJ, 624, 436

Lamberts T., Cuppen H. M., Ioppolo S., Linnartz H., 2013, PCCP, 15, 8287

Łapiński A., Spanget-Larsen J., Waluk J., Radziszewski J. G., 2001, JCP, 115, 1757

Lin C. L., Leu M. T., 1982, Int. J. Chem. Kinet., 14, 417

Linnartz H. *et al*., 2011, in IAU Symposium, edited by J. Cernicharo and R. Bachiller (2011), 280, 390

Loeffler M. J., Baratta G. A., Palumbo M. E., Strazzulla G., Baragiola R. A., 2005, A&A, 435, 587

Madzunkov S., Shortt B. J., Macaskill J. A., Darrach M. R., Chutjian A., 2006, Phys. Rev. A, 73, 020901

Markwalder B., Gozel P., van den Bergh H., 1993, JCP, 97, 5260

Matar E., Congiu E., Dulieu F., Momeni A., Lemaire J. L., 2008, A&A, 492, L17

Mennella V., Baratta G. A., Palumbo M. E., Bergin E. A., 2006, ApJ, 643, 923

Mennella V., Palumbo M. E., Baratta G. A., 2004, ApJ, 615, 1073

Miyauchi N., Hidaka H., Chigai T., Nagaoka A., Watanabe N., Kouchi A., 2008, Chem. Phys. Lett., 456, 27

Mokrane H., Chaabouni H., Accolla M., Congiu E., Dulieu F., Chehrouri M., Lemaire J. L., 2009, ApJL, 705, L195

Moore M. H., Khanna R., Donn B., 1991, J. Geophys. Res., 96, 17541

Noble J. A., Dulieu F., Congiu E., Fraser H. J., 2011, ApJ, 735, 121

Nour E. M., Chen L. H., Laane J., 1983, J. Phys. Chem., 87, 1113

Nour E. M., Chen L. H., Strube M. M., Laane J., 1984, J. Phys. Chem., 88, 756

Oba Y., Watanabe N., Kouchi A., Hama T., Pirronello V., 2010a, ApJL, 712, L174

Oba Y., Watanabe N., Kouchi A., Hama T., Pirronello V., 2010b, ApJ, 722, 1598

Öberg K. I., Boogert A. C. A., Pontoppidan K. M., van den Broek S., van Dishoeck E. F., Bottinelli S., Blake G. A., Evans II N. J., 2011, ApJ, 740, 109

Palumbo M. E., Baratta G. A., Brucato J. R., Castorina A. C., Satorre M. A., Strazzulla G., 1998, A&A, 334, 247

Raut U., Baragiola R. A., 2011, ApJL, 737, L14

Raut U., D. Fulvio, M. J. Loeffler, R. A. Baragiola, 2012, ApJ, 752, 159

Romanzin C., Ioppolo S., Cuppen H. M., van Dishoeck E. F., Linnartz H., 2011, JCP, 134, 084504

Roser J. E., Vidali G., Manrico G., Pirronello V., 2001, ApJ, 555, L61

Ruffle D. P., Herbst E., 2001, MNRAS, 324, 1054

Sandford S. A., Allamandola L. J., Tielens A. G. G. M., Valero G. J., 1988, ApJ, 329, 498

Satorre M. A., Palumbo M. E., Strazzulla G., 2000, Astrophys. & Space Sci., 274, 643

Schieferstein M., Kohse-Höinghaus K., Stuhl F., 1983, Ber. Bunsenges. Phys. Chem., 87, 361

Sivaraman B., Mebel A. M., Mason N. J., Babikov D., Kaiser R. I., 2011, PCCP (Incorporating Faraday Transactions), 13, 421

Slanger T. G., Wood B. J., Black G., 1972, JCP, 57, 233

Talbi D., Chandler G. S., Rohl A. L., 2006, Chem. Phys., 320, 214

Teolis B. D., Loeffler M. J., Raut U., Fama M., Baragiola R. A., 2007, Icarus, 190, 274

Tschersich K. G., 2000, J. Appl. Phys., 87, 2565

Tschersich K. G., Fleischhauer J. P., Schuler H., 2008, J. Appl. Phys., 104, 034908

Tschersich K. G., von Bonin V., 1998, J. Appl. Phys., 84, 4065

van Dishoeck E. F. *et al*., 1996, A&A, 315, L349

Watanabe N., Hidaka H., Kouchi A., 2006, in Astrochemistry - From Laboratory Studies to Astronomical Observations, edited by R. I. Kaiser, P. Bernath, Y. Osamura, S. Petrie, and A. M. Mebel, vol. 855 of AIP Conf. Ser., pp. 122–127.

Watanabe N., Kouchi A., 2002a, ApJL, 571, L173

Watanabe N., Kouchi A., 2002b, ApJ, 567, 651

Wohar M. M., Jagodzinski P. W., 1991, J. Molec. Spectrosc., 148, 13